American Mineralogist, Volume 81, pages 1380–1395, 1996

HRTEM of microcrystalline opal in chert and porcelanite from the Monterey Formation, California

S.L. Cady,[1] H.-R. Wenk,[2] and K.H. Downing[3]

[1]NASA Ames Research Center, Moffett Field, California 94035, U.S.A.
[2]Department of Geology and Geophysics, University of California, Berkeley, California 94720, U.S.A.
[3]Life Sciences Division, Lawrence Berkeley National Laboratory, Berkeley, California 94720, U.S.A.

Abstract

Microcrystalline opal was investigated using low-dose transmission electron microscopy (TEM) methods to identify microstructural characteristics and possible phase-transformation mechanisms that accommodate silica diagenesis. High-resolution TEM (HRTEM) revealed that microcrystalline opal in opal-CT chert (>90 wt% silica) and opal-CT porcelanite (50–90 wt% silica) from the Miocene Monterey Formation of California displays various amounts of structural disorder and coherent and incoherent lamellar intergrowths. Species of microfibrous opal identified by HRTEM in early-formed opal-CT chert include length-slow opal-C and unidimensionally disordered length-slow opal-CT ("lussatite"). These fibers often display a microstructure characterized by an aperiodic distribution of highly strained domains that separate ordered domains located at discrete positions along the direction of the fiber axes. Microfibrous opal occurs as several types of fiber-aggregation forms. TEM revealed that the siliceous matrix in later-formed opal-CT porcelanite consists of equidimensional, nanometer-size opal-CT crystallites and lussatite fibers. Pseudo-orthorhombic tridymite (PO-2) was identified by HRTEM in one sample of opal-CT porcelanite. Burial diagenesis of chert and porcelanite results in the precipitation of opal-C and the epitaxial growth of opal-C domains on opal-CT substrates. Diagenetic maturation of lussatite was identified by TEM in banded opal-CT–quartz chert to occur as a result of solid-state ordering. The primary diagenetic silica phase transformations between noncrystalline opal, microcrystalline opal, and quartz occur predominantly by a series of dissolution-precipitation reactions. However, TEM showed that in banded opal-CT–quartz chert, the epitaxial growth of quartz on microfibrous opal enhances the rate of silica diagenesis.

Introduction

Microcrystalline opal most commonly forms in biosiliceous marine sediments as a result of the crystallization of opal-A, a biogenically precipitated form of noncrystalline silica (e.g., Hesse 1988). Although quartz is the thermodynamically favored silica phase at near-surface conditions, kinetic factors promote the formation of microcrystalline opal after the dissolution of opal-A (Mizutani 1966, 1977; Kastner et al. 1977; Tada and Iijima 1982; Kastner and Gieskes 1983; Williams et al. 1985; Williams and Crerar 1985; Morse and Casey 1988). The paragenetic sequence of silica phases that form during the burial diagenesis of biosiliceous marine sediments includes noncrystalline opal (opal-A, which is biogenically precipitated; opal-A′, which is inorganically precipitated, terminology of Hein et al. 1978), microcrystalline opal (opal-CT, disordered low cristobalite–low tridymite; opal-C, ordered low cristobalite with minor amounts of low tridymite), and microcrystalline quartz (which may include varieties of fibrous quartz). All stages of silica diagenesis can be found in the hemipelagic biosiliceous deposits of the Monterey Formation of California (e.g., Isaacs et al. 1983).

Biosiliceous deposits of the Monterey Formation accumulated during the Miocene in continental borderland basins along the coast of California. The early petrographic studies of Bramlette (1946) and the geochemical and X-ray diffraction (XRD) investigations of Murata and coworkers (Murata and Nakata 1974; Murata and Larson 1975; Murata and Randall 1975; Murata et al. 1977) provided the basis for numerous studies of the Monterey Formation (e.g., Isaacs 1981a, 1982; Garrison et al. 1981; Pisciotto and Garrison 1981; Isaacs and Garrison 1983; Keller and McGowen 1990; Schwalbach and Bohacs 1993; Garrison and Ingle 1985; Behl and Garrison 1994). Variation in basin topography and in the position and intensity of the O_2-minimum zone within individual basins resulted in differences in depositional environments and bulk sediment composition.

Although temperature is the dominant factor controlling the rates of silica diagenesis, field studies have shown that the amount of terrigenous material present in

0003–004X/96/1112–1380$05.00

the initial biosiliceous sediment had a significant influence on the timing of the formation of the diagenetic silica phases in the Monterey Formation (Isaacs 1982; Keller and Isaacs 1985; Behl and Garrison 1994). Experimental studies have also shown that the presence of clay and organic matter delays the rate of transformation between noncrystalline and microcrystalline opal but enhances the transformation rate between microcrystalline opal and quartz (Kastner et al. 1977; Hinman 1990). Kastner et al. (1977) demonstrated experimentally that geochemical factors can even reverse diagenetic trends. In general, microcrystalline opal forms in highly siliceous chert (>90 wt% silica) at lower temperatures than in detrital-rich porcelanite (50–90 wt% silica) and siliceous mudstone (<50 wt% silica) (e.g., Isaacs 1982; Behl and Garrison 1994).

Detailed XRD studies have shown that several changes occur in the powder XRD pattern of microcrystalline opal as a result of burial diagenesis. These changes include a decrease in the primary *d* value, the appearance of additional cristobalite reflections, a decrease in the relative diffraction intensity of one of the reflections attributed exclusively to tridymite, and an overall peak-sharpening effect. Murata and Nakata (1974) interpreted the changes in the powder XRD pattern as an indication that microcrystalline opal in porcelanite gradually transforms during diagenesis from the more disordered species, opal-CT, to the more ordered species, opal-C (e.g., Murata and Randall 1975; Isaacs 1981a; Pisciotto 1981). This apparent structural transformation coincides with an increase in the crystallinity of microcrystalline opal. Debate continues regarding the mechanism responsible for the apparent structural phase transformation that occurs during diagenesis.

Two mechanisms have been proposed to accommodate the transformation of opal-CT to opal-C during diagenesis. On the basis of ^{18}O isotope studies, Murata et al. (1977) proposed that opal-CT transforms to opal-C in the solid state. Within the stratigraphic zone where opal-CT converts to cristobalitic opal, the ^{18}O isotope signatures remain fairly constant. The ^{18}O isotope signatures decrease in a stepwise manner across the interzonal sediment boundaries where the primary silica phase transformations occur between noncrystalline opal, microcrystalline opal, and quartz. However, Williams et al. (1985) proposed that the increase in crystallinity observed in powder XRD patterns of microcrystalline opal during diagenesis is due to Ostwald ripening. The driving force for Ostwald ripening is the gradual reduction of interfacial surface area between crystals and solution as a result of the simultaneous dissolution of smaller crystals and the growth of larger ones within the same medium (e.g., Baronnet 1982; Morse and Casey 1988; Steefel and Van Cappellen 1990). Williams and Crerar (1985) argued that a solid-state transformation in microcrystalline opal is unlikely because solid-state diffusion reactions are prohibitively slow during early diagenesis.

To contribute to an understanding of the structure and diagenetic behavior of microcrystalline opal, we investigated microstructural and morphological characteristics with low-dose, conventional and high-resolution TEM methods. We compared diagenetic microcrystalline opal that formed in opal-CT chert with samples that formed in opal-CT porcelanite from the Monterey Formation of California.

Microcrystalline opal

Our current understanding of the structure of microcrystalline opal comes from the work of Flörke (1955, 1967) and his coworkers (Flörke et al. 1975, 1976, 1990, 1991; Graetsch et al. 1985, 1987, 1994; Graetsch and Flörke 1991). Flörke (1955) proposed that the structure of microcrystalline opal consists predominantly of unidimensionally disordered low cristobalite with varying amounts of interstratified tridymite-type stacking sequences. Species of microcrystalline opal are classified on the basis of their powder XRD patterns (Jones and Segnit 1971; Graetsch et al. 1994). Opal-CT produces a pattern that contains three broadened reflections: a primary reflection centered near 4.1 Å, a secondary reflection at about 4.3 Å, and a subsidiary reflection at about 2.5 Å. Because of the similarities in the *d* values of low cristobalite and low tridymite (Table 1), only the secondary reflection in opal-CT powder XRD patterns at about 4.3 Å is attributed exclusively to low tridymite (Flörke 1955). Opal-C produces a powder XRD pattern that contains additional medium and weak low cristobalite reflections and low tridymite reflections at 4.3 and 3.9 Å. However, the relative difference in intensity between low tridymite and low cristobalite reflections is greater in the powder XRD pattern of opal-C than in that of opal-CT (Graetsch and Flörke 1991).

Flörke's (1955) unidimensionally disordered cristobalite model has been successfully used to simulate powder XRD patterns, which have then been compared with the powder XRD patterns of several opaline silica samples (Graetsch and Flörke 1991; Graetsch et al. 1994). These studies concluded that the disordered opal-CT structure can contain between 30 and 50% tridymite-type stacking disorder, and that the opal-C structure can contain between 20 and 30% tridymite-type stacking disorder. Guthrie et al. (1995) recently expanded this type of modeling approach to accommodate different types of ordering interstratifications when calculating powder XRD patterns of microcrystalline opal. A comparison of simulated powder XRD patterns with those measured from opal-CT samples suggests that the structure of opal-CT contains partially ordered interstratifications of tridymite and cristobalite (Guthrie et al. 1995). In each of the studies, idealized high cristobalite and high tridymite structures were used for simplicity to simulate powder XRD patterns.

The high-temperature cristobalite and tridymite structures are similar in that both consist of stacking sequences built of layers that contain interconnected, six-membered rings of silica tetrahedra. In the idealized high-temperature cristobalite and tridymite structures (i.e., 180° Si-

TABLE 1. X-ray powder data for cristobalite and tridymite modifications

High CR			Low CR			TR PO (5/10)			TR-MC			High TR		
d (Å)	I/I_o	*hkl*	*d* (Å)	I/I_o	*hkl*	*d* (Å)	I/I_o	*hkl*	*d* (Å)	I/I_o	*hkl*	*d* (Å)	I/I_o	*hkil*
—	—	—	—	—	—	—	—	—	—	—	—	4.38	100	$10\bar{1}0$
—	—	—	—	—	—	—	—	—	4.32	100	$\bar{1}13$	—	—	—
—	—	—	—	—	—	4.30	100	220	—	—	—	—	—	—
4.15	100	111	—	—	—	—	—	—	—	—	—	—	—	—
—	—	—	—	—	—	—	—	—	—	—	—	4.14	55	0002
—	—	—	—	—	—	4.09	96	00$\underline{2}$0	4.09	83	400	—	—	—
—	—	—	4.05	100	101	—	—	—	—	—	—	—	—	—
—	—	—	—	—	—	—	—	—	—	—	—	3.87	55	$10\bar{1}1$
—	—	—	—	—	—	—	—	—	3.82	54	$\bar{3}13/113$	—	—	—
—	—	—	—	—	—	3.81	56	22$\underline{1}$0	—	—	—	—	—	—
—	—	—	—	—	—	3.25	20	2$\underline{4}$0	—	—	—	—	—	—
—	—	—	3.14	12	111	—	—	—	—	—	—	—	—	—
—	—	—	—	—	—	—	—	—	—	—	—	3.01	18	$10\bar{1}2$
—	—	—	—	—	—	2.97	16	22$\underline{2}$0	2.97	14	$\bar{5}13/313$	—	—	—
—	—	—	2.84	14	102	—	—	—	—	—	—	—	—	—
2.53	80	220	—	—	—	—	—	—	—	—	—	2.53	23	$11\bar{2}0$
—	—	—	—	—	—	—	—	—	2.50	22	020	—	—	—
—	—	—	2.49	20	200	—	—	—	—	—	—	—	—	—
—	—	—	—	—	—	2.48	13	260	—	—	—	—	—	—
—	—	—	—	—	—	—	—	—	—	—	—	2.33	11	$10\bar{1}3$
2.17	10	311	—	—	—	—	—	—	—	—	—	—	—	—
2.07	30	222	—	—	—	—	—	—	—	—	—	—	—	—

Note: Low cristobalite (Low CR) diffractometer data from PDF 11-695; tetragonal, $a = 4.97$, $c = 6.92$ Å. High cristobalite (High CR) at 500 °C, powder cameral data from PDF 4-359; cubic, $a = 7.18$ Å. Tridymite (low, PO 5/10; low, MC) and high tridymite (High TR) diffractometer data from Graetsch and Flörke 1991. PO 5/10 abbreviation for pseudo-orthorhombic ("terrestrial") tridymite-5/10 stacking sequence along *c**, MC abbreviation for monoclinic ("meteoritic") tridymite. I/I_o is intensity normalized to the strongest peak equal to 100.

-O-Si bond angles), the six-membered rings within the layers have a hexagonal shape in projection. In cubic high cristobalite each stacking sequence consists of three layers stacked in the <111> direction. The silica tetrahedra within the layers are stacked in a cubic close-packed arrangement. In hexagonal high tridymite each stacking sequence contains only two layers stacked along [0001]. The silica tetrahedra within these layers are stacked in a hexagonal close-packed arrangement. Displacive transformations characterize the high-low structural transitions of all silica polymorphs (e.g., Heaney 1994).

In the low-temperature cristobalite and tridymite structures, the six-membered rings project either as ditrigons (D rings) or as ovals (O rings) when viewed parallel to the stacking direction (e.g., Wennemer and Thompson 1984; Heaney 1994). Only six-membered O rings characterize the topologically similar structures of tetragonal low cristobalite (Dollase 1965; Peacor 1973) and the numerous polytypes of pseudo-orthorhombic (PO-*n*) low tridymite (Konnert and Appleman 1978; Nukui and Nakazawa 1980). The polytypic structures of two additional low tridymite polymorphs display monoclinic symmetry with layers that contain either a combination of O rings and D rings (MC) (Dollase and Baur 1976; Kato and Nukui 1976; Baur 1977) or only D rings (Löns and Hoffman 1987). Structural intergrowths of all three low-temperature tridymite structural modifications, with or without cristobalite, have been identified in synthetic and natural crystals of low tridymite (e.g., Schneider and Flörke 1986; Nukui and Flörke 1987). In the present study, electron diffraction patterns produced by species of microcrystalline opal were indexed using the unit cell of low cristobalite; the *d* values of related tridymite reflections are given in Table 1.

Graetsch et al. (1994) recently studied a variety of samples of microcrystalline opal that contain various degrees of disorder, using ^{29}Si MAS NMR spectroscopy, infrared-absorption spectroscopy, and XRD. The authors found that increased distortion in the local arrangement of silica tetrahedra is due to the incorporation of OH and molecular H_2O and to the presence of stacking disorder. H_2O is the major impurity in microcrystalline opal, present in amounts between 1 and 3 wt% in opal-C and between 3 and 10 wt% in opal-CT (Langer and Flörke 1974; Graetsch et al. 1985; Flörke et al. 1991). The presence of variable amounts of stacking disorder and significant amounts of impurities contributes to the problems associated with characterizing the structure of microcrystalline opal.

MATERIALS AND METHODS

Samples of banded opal-CT–quartz chert and opal-CT porcelanite from exposed sections of the Monterey Formation west of Santa Barbara, California, between Goleta and Point Arguello, were provided by C.M. Isaacs, R.W. Murray, and K.A. Pisciotto. Samples of banded opal-CT–quartz chert are characterized by laminae of microquartz (1–5 mm thick) separated by thinner laminae of opal-CT (<1 mm thick). Relatively pure opal-CT laminae (<0.5 mm thick) usually lie adjacent to laminae containing microquartz, whereas less pure opal-CT laminae (<3 mm thick), containing minor amounts of clay (illite) and carbonate (dolomite rhombohedra), usually lie between the sequences of microquartz and pure opal-CT laminae.

Samples of banded opal-CT–quartz chert were used in this study because they contain the two principal diagenetic silica phases and the transformation boundary between the two phases could be studied in detail. XRD analysis indicated that the primary *d* value of opal-CT crystallites in the banded opal-CT–quartz chert is approximately 4.09 Å. Fine-scale laminations in the opal-CT porcelanite samples are caused by varying proportions of detrital material and organic matter relative to biosiliceous debris. Petrographically, opal-CT porcelanite appears pseudoisotropic under crossed nicols because of the submicroscopic grain size of the silica and clay minerals. Opal-CT porcelanite samples selected for this study represent progressively more advanced stages of diagenetic maturation, determined from powder XRD measurements of the primary *d* value for each opal-CT sample (4.06–4.11 Å).

It is important to note that, historically, siliceous sedimentary rocks have been named on the basis of differences in surface texture and physical properties (Bramlette 1946). Because rocks that contain significantly different proportions of diagenetic silica phases can have a similar appearance (Isaacs 1981b; Dunham and Blake 1987), mineral modifiers should be added to the rock names after XRD analysis.

TEM foils were prepared by ion milling petrographic thin sections prepared from bulk samples. Bulk samples were cut into cubes (1–2 cm^3), embedded under vacuum in an epoxy resin (Epotek), and cured at room temperature for 2 d. Sections were cut both parallel and perpendicular to bedding-plane laminations. Phase-contrast lattice-fringe images were acquired at Scherzer focus (e.g., Buseck et al. 1988). Lattice-fringe spacings were measured on optical diffractograms obtained by taking the Fourier transform of individual crystallites from high-resolution transmission electron microscopy (HRTEM) negatives.

Although silica polymorphs are sensitive to electron irradiation, the use of low-dose imaging made it possible to obtain phase-contrast images of diagenetic microcrystalline opal. Low-dose HRTEM was performed using a JEOL 4000FX transmission electron microscope operating at 400 keV. The protocol used for low-dose imaging in this study, as described below, was developed for the HRTEM investigation of proteins (Downing 1991; Downing et al. 1992). Thicker sections of electron-transparent foils were examined using conventional TEM methods with a Kratos high-voltage transmission electron microscope operating at a maximum accelerating voltage of 1.5 MeV. Higher accelerating voltages (up to 650 keV) have been shown to reduce the rate of beam damage in quartz (Das and Mitchell 1974).

Two types of damage produce irreversible changes in the atomic structures of materials in a transmission electron microscope during electron-beam irradiation (e.g., Hobbs 1985). "Knock-on" damage involves the direct transfer of momentum from the incident electron to an atom in the specimen, ultimately producing atomic displacements. Radiolytic damage, or radiolysis, involves a momentum-energy conversion that can break bonds and produce local changes in the atomic coordination. Atomic rearrangements caused by radiolysis may eventually lead to the amorphization of crystalline structures. Structural considerations suggest that radiolysis is the primary cause of irradiation damage to all silica polymorphs in the transmission electron microscope (Hobbs 1979). The presence of adsorbed OH groups also sensitizes microcrystalline opal to radiolytic damage because weaker Si-OH:HO-Si hydrolyzed bonds radiolyze more easily than stronger Si-O-Si bonds (e.g., Pascucci et al. 1983).

The loss of structural integrity in microcrystalline opal was documented by us in electron diffraction patterns and HRTEM lattice-fringe images. In electron diffraction patterns recorded from a region of the sample containing several randomly oriented fibers of microcrystalline opal (Figs. 1A–1C), structural damage caused by prolonged beam exposure results in the loss of most high-order reflections and many of the weaker reflections located in the intense, primary 4.1 Å diffraction ring. HRTEM lattice-fringe micrographs of microcrystalline opal (Figs. 1D–1F) show that irradiation-induced amorphization occurs initially at the crystal surfaces and where crystals are in contact with one another. Lattice-fringe contrast in the crystals diminishes as amorphization proceeds inward.

Exposure of specimens to a critical dose of electron irradiation during investigation in a transmission electron microscope prevents detailed structural analysis of irradiation-sensitive materials using conventional TEM methods. Minimum-exposure methods were originally developed to limit beam damage by exposing a specimen to irradiation only during image recording (e.g., Williams and Fisher 1970). An area adjacent to the area of interest was focused, and then the sample was manually translated to a pristine area for image recording. However, because of problems associated with rapid sample heating, residual stage motion, or a change in focus resulting from sample translation, such methods have been replaced by automated low-dose techniques. The protocol implemented in this study used computer-controlled lenses. As a result, a specimen could be searched and focused at lower magnifications using a low beam intensity, and then the electron beam rather than the sample could be tilted to expose an adjacent pristine area during image recording.

Two types of low-dose imaging procedures were used to obtain HRTEM micrographs in this study. Spot-scanned images were produced by rastering a condensed electron beam over the specimen (e.g., Downing 1991). The contrast in spot-scanned images varies periodically because of beam overlap when the sample is rastered. Low-dose images were also acquired by using a decondensed beam to retain constant image intensity. Comparisons made using both techniques on several different areas of the specimens revealed that in the flood-beam images, localized specimen charging resulted in a loss of

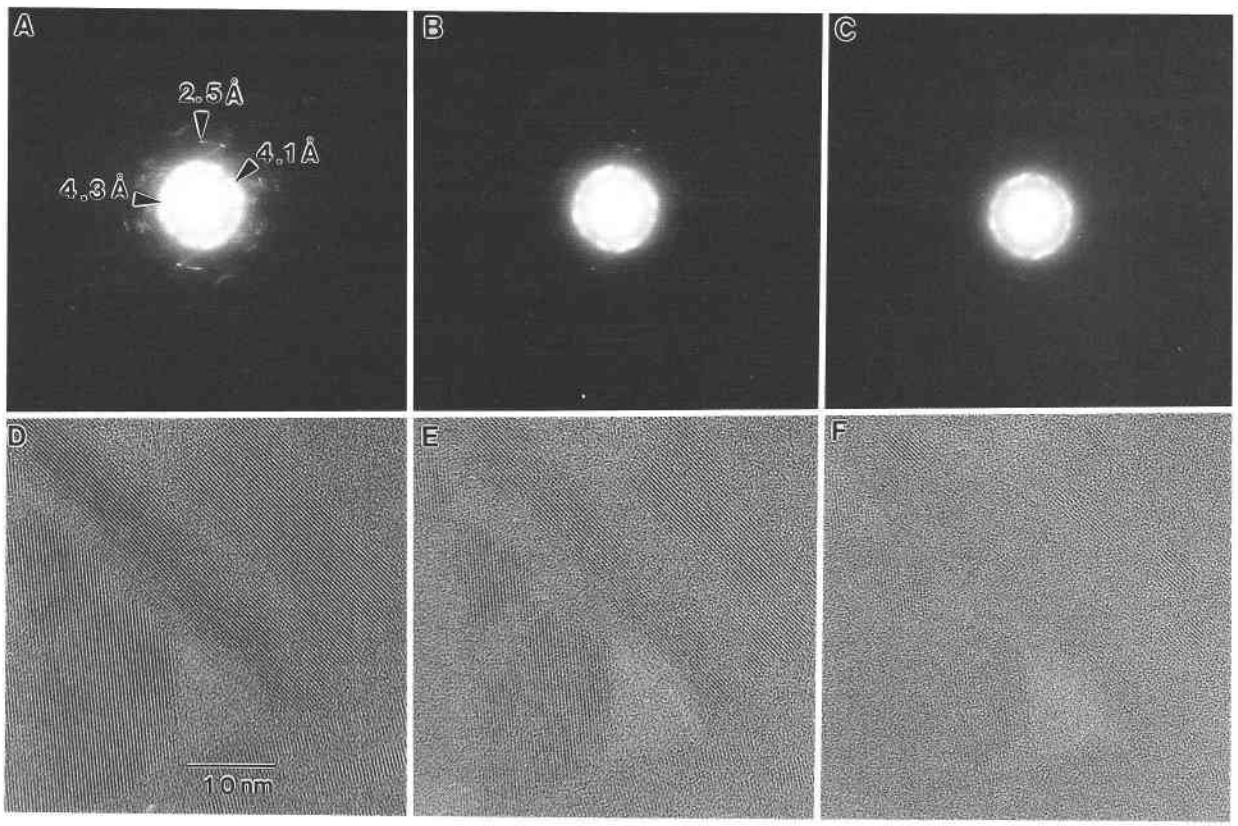

FIGURE 1. Effects of electron-beam irradiation damage in microcrystalline opal. Loss of diffraction contrast recorded in SAED patterns taken (**A**) 5 s, (**B**) 150 s, and (**C**) 270 s after initial beam exposure. Exposure rate: 1020 e/(nm²·s). Amorphous transformation recorded in lattice-fringe HRTEM micrographs taken (**D**) 2 s, (**E**) 45 s, and (**F**) 120 s after initial beam exposure. Exposure rate: 70 e/(nm²·s). Series of diffraction patterns and micrographs acquired at 400 keV accelerating voltage.

resolution evidenced by anisotropy in the Fourier transforms of the HRTEM micrographs. Specimen charging produces an effect similar to specimen drift except that the loss of resolution owing to specimen charging changes direction in the HRTEM micrograph.

OBSERVATIONS BY CONVENTIONAL TEM

Under conditions of uninhibited growth, microspherical aggregates (>2 μm in diameter) of opal-CT commonly line the walls of open cavities in porous biosiliceous sediments (e.g., Oehler 1975; Flörke et al. 1975). Microspherical aggregates composed of platy, blade-shaped crystals are referred to as lepispheres, meaning spheres of blades (Weaver and Wise 1972). Flörke et al. (1976), on the basis of morphological evidence and crystallographic considerations, proposed that opal-CT lepispheres are composed of platelets or blades oriented parallel to {111} (cubic setting) of cristobalite and {0001} (hexagonal setting) of tridymite. These platelets or blades are intergrown according to the $(30\bar{3}4)$ and $(10\bar{1}6)$ twin laws of tridymite (Flörke et al. 1976). Scanning electron microscopy (SEM) has been used to show that opal-CT lepispheres in siliceous deep-sea sediments display a variety of surface textures (Weaver and Wise 1972; Wise et al. 1972; Rad and Rösch 1972; Hein et al. 1981). However, opaline silica grains that occur in the matrix of siliceous deep-sea sediment and that lack any distinctive morphology are referred to as having a massive form (Keene 1975). Because of the fine grain size, microcrystalline opal that formed within the matrix of biosiliceous sediment of the Monterey Formation also appears rather featureless in SEM micrographs (e.g., Isaacs et al. 1983). Conventional TEM, however, revealed that the cryptocrystalline opaline matrix in chert and porcelanite of the Monterey Formation contains a variety of fiber-aggregation forms.

Microcrystalline opal in banded opal-CT–quartz chert

In opal-CT laminae of banded chert, microcrystalline opal occurs as isolated acicular fibers up to 250 nm in length (Figs. 2A and 2B). Fibers of microcrystalline opal are randomly oriented in the matrix and produce an electron diffraction pattern that consists of a set of concentric diffraction rings. The intense primary ring contains strong individual reflections from cristobalite-type (4.1 Å) and tridymite-type (4.3 Å) domains (inset, Fig. 2A). Both domains produce sharp 2.5 Å reflections in the weaker secondary diffraction ring. Some of the fibers contain

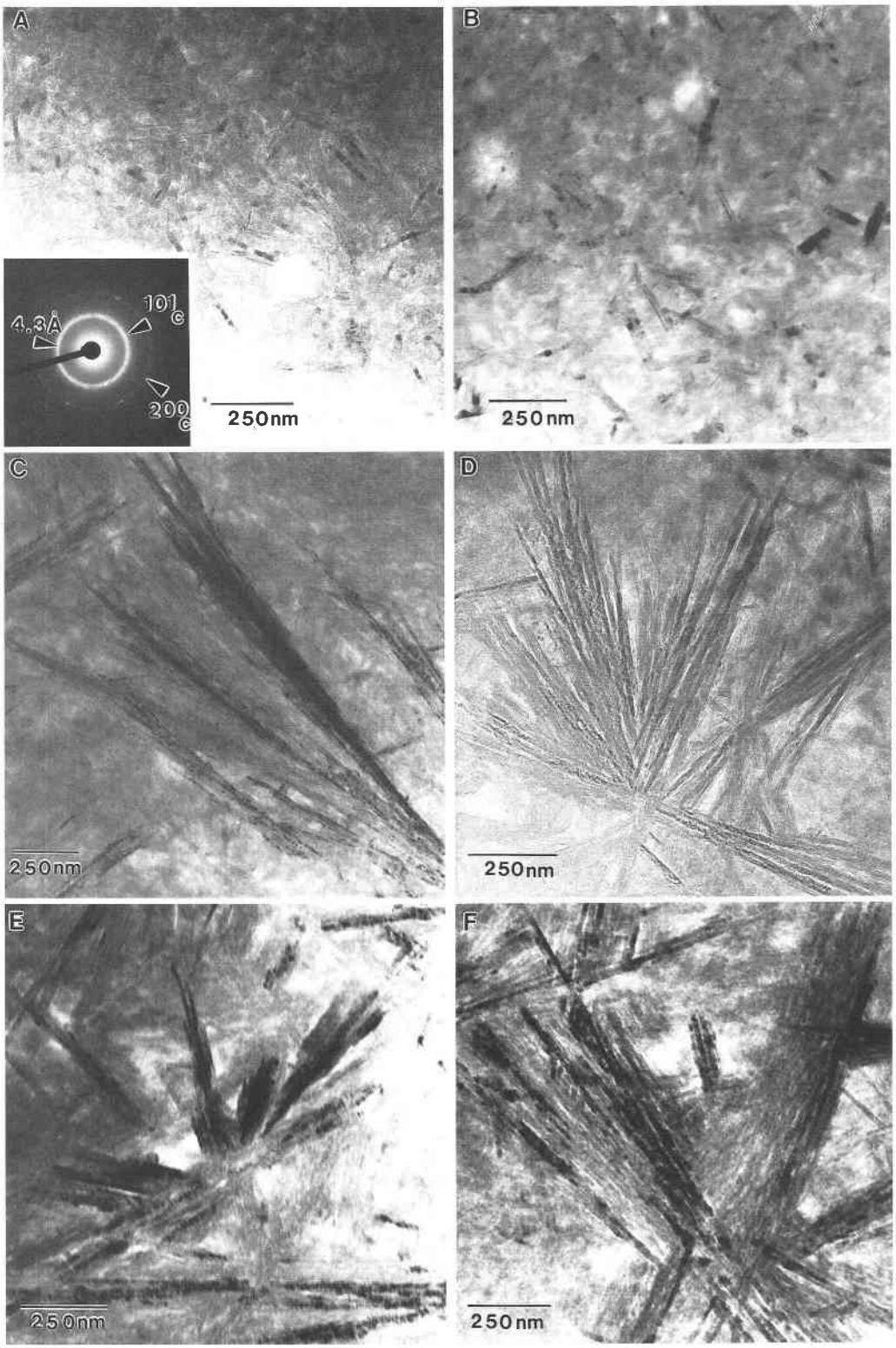

FIGURE 2. Inset in **A** shows SAED pattern of opal-CT. Bright-field TEM micrographs of microfibrous opal in matrix of banded opal-CT–quartz chert display (**A**) mottled diffraction contrast and (**B**) mottled and lamellar diffraction contrast. Fiber-aggregation forms include (**C**) radially divergent fiber bundles, (**D**) rosettes, (**E**) embryonic spherulites composed of randomly divergent fiber bundles, and (**F**) crystallographically controlled interpenetrating fibers.

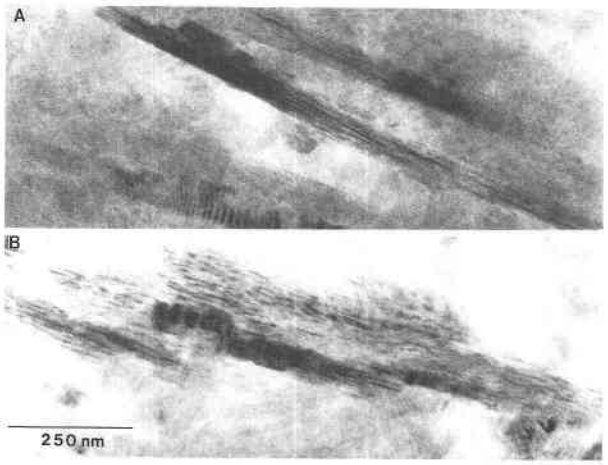

FIGURE 3. Bright-field TEM micrograph showing structurally ordered microfibrous opal characterized by (**A**) coherent lamellar domains and (**B**) incoherent lamellar domains. Loss of diffraction contrast in interlamellar regions is due to increase in local disorder between ordered lamellar domains.

FIGURE 4. Bright-field TEM micrograph showing epitaxially grown quartz crystals (labeled q) on substrate of microfibrous opal. Newly formed quartz grains display highly strained diffraction contrast. SAED pattern in inset reveals preferred orientation of quartz crystals presumably inherited from topotaxially transformed microfibrous opal.

strongly diffracting lamellar domains (Fig. 2B). The stacking direction of these lamellar domains lies perpendicular to the fiber axes. The microstructure of other opal-CT fibers consists of smaller, nonlamellar domains. The presence of several nonlamellar domains within any one individual fiber gives them a mottled diffraction contrast in bright-field TEM micrographs. The structure of the lamellar and nonlamellar domains could not be analyzed using convergent-beam electron diffraction because of the sensitivity of opaline silica to electron-beam irradiation damage.

Fiber-aggregation forms of microcrystalline opal in opal-CT–bearing laminae of the banded opal-CT–quartz chert include radially divergent fiber bundles, rosettes, and embryonic spherulites (Figs. 2C–2F). The longitudinal growth of individual fibers within the fiber-aggregation forms varies, giving the tips of the fiber bundles a variegated texture. Moiré fringes located along the boundaries of overlapping fibers in the rosette (Fig. 2D) are caused by their structural misorientation. Embryonic spherulites often contain several fiber bundles that diverge in several seemingly random directions away from the central nuclei (Fig. 2E). In any one growth direction, closely spaced fibers in each fiber bundle remain approximately parallel to one another. Distinct sets of interpenetrating fibers characterize other embryonic spherulites (Fig. 2F). In these spherulites, fiber growth is crystallographically controlled at the nucleus. Individual sets of fibers diverge approximately 65–75° away from one another. This range of divergence angles includes the interplanar angle between the {101} lattice planes of low cristobalite. Although many of the fibers in this embryonic spherulite are tilted out of a diffracting orientation, pore space between the fibers remains visible.

TEM micrographs revealed that at the boundaries between opal-CT and quartz laminae in banded chert, microfibrous opal becomes structurally more ordered. Solid-state structural ordering is evidenced by an increase in the number of distinct, strongly diffracting lamellar domains that are stacked perpendicular to the fiber axis (Fig. 3A). The lamellar domains terminate laterally within the acicular fibers. Fibers that have less well-defined grain boundaries also display more finite lamellar domains (Fig. 3B). However, these lamellar domains are shorter, and they often lie subparallel to one another and have nonplanar boundaries. Both types of lamellar domains vary in width (<1–10 nm). Microfibrous opal that becomes structurally more ordered also displays less diffraction contrast from interlamellar regions. The loss of diffraction contrast from the interlamellar regions is interpreted to result from an increase in disorder between the ordered lamellar domains during structural reordering.

Evidence for the epitaxial growth of quartz on opal-CT at the opal-CT–quartz laminae boundaries in banded chert is shown in Figure 4. Newly formed quartz domains are located along discrete sections of opal-CT fibers. High concentrations of Brazil twins characterize the microstructure of diagenetic microcrystalline quartz (Cady et al. 1993). The growth and coalescence of several quartz crystals produced an irregular diffraction contrast in the central region of the TEM micrograph under bright-field imaging conditions. However, a selected-area electron diffraction (SAED) pattern of the coalesced quartz grains revealed that they have a similar orientation, presumably controlled by the orientation of a microfibrous opal-CT substrate. The epitaxial nucleation of quartz on opal-CT is interpreted to lead to the eventual topotaxial conversion of opal-CT to quartz (e.g., Wenk et al. 1988).

Microcrystalline opal in opal-CT porcelanite

Microcrystalline opal that forms in finely laminated porcelanite was also investigated using conventional TEM methods. Microcrystalline opal initially precipitates as nanometer-size crystallites with an equidimensional habit (Fig. 5A). These crystallites form the finest-grained portion of the sediment and surround the larger clay particles with a dense matrix of diagenetic silica. Previous studies have shown that an increase in the bulk density of the sediment and a reduction of up to 50% in sediment porosity are associated with the occurrence of detectable amounts of opal-CT in porcelanite when analyzed using powder XRD methods (Isaacs 1981c). In bright-field TEM micrographs the opal-CT crystallites display a mottled appearance. These opal-CT crystallites produce a set of diffuse but well-defined diffraction rings in the SAED pattern (inset, Fig. 5A). The diffuse nature of the primary diffraction ring may be due either to the high concentration of stacking faults in the opal-CT crystallites or to the presence of tridymite-type domains (e.g., Graetsch et al. 1987). As noted by Flörke et al. (1991), stacking faults in cristobalite and tridymite produce diffuse low-angle diffraction intensity in the stacking direction at about 4.3 Å (e.g., Jagodzinski and Laves 1948; Jagodzinski 1949a, 1949b, 1949c). A ratio of the average d value of the primary and the secondary opal-CT diffraction rings indicates that these opal-CT crystallites are better approximated by a low cristobalite rather than a high cristobalite structure. Intense reflections scattered between the opal-CT diffraction rings are attributed to larger clay particles. Clay particles also contribute a diffuse halo superimposed on the opal-CT diffraction rings.

Microfibrous opal that forms in the matrix of opal-CT porcelanite is often associated with the recrystallized remains of microfossils. As shown in Figure 5B, the opal-CT fibers project radially outward from the remains of a circularly shaped microfossil cavity. The center of the cavity is infilled with smaller, more equidimensional opal-CT crystallites. The primary silica phase transformations generally occur earlier in recrystallized diatom frustules than in the sediment matrix (Isaacs 1981b). We interpret the presence of acicular opal-CT fibers as evidence that, subsequent to opal-CT nucleation, relatively rapid dissolution of the primary biogenic opal in the microfossil promoted the growth of microfibrous opal. The presence of biogenic carbonate debris also promotes opal-CT nucleation (Kastner et al. 1977; Hinman 1990). However, elemental analysis using an energy-dispersive spectrometer revealed that this microfossil contains only silica.

Newly formed, anhedral opal-C crystals were identified using dark-field analysis in areas around recrystallized microfossils. In Figure 5C, the radial sector of a microfossil that contains anhedral opal-C crystals in the region formerly occupied by a dense rind of opal-CT fibers is oriented for comparison with Figure 5B. The corresponding SAED pattern from this area contains additional reflections used for dark-field analysis that correspond to the {111} and {102} d values of low cristobalite (Fig. 5E). Opal-C crystals around the microfossil vary in grain size and do not appear to be associated with any fibrous precursor. However, a few of the remaining opal-CT fibers that lie perpendicular to the microfossil cavity are associated with subhedral overgrowths of a more ordered phase.

Structural ordering of opal-CT fibers in opal-CT porcelanite occurs during later stages of crystal growth. In the dark-field TEM micrograph shown in Figure 5D, opal-C domains that display a relatively unmottled diffraction contrast (see arrows) are located along the outermost portions of the closely spaced opal-CT fibers. The corresponding SAED pattern produced by this region of the specimen (Fig. 5F) includes additional low cristobalite reflections used to produce the dark-field TEM micrograph. Many of the opal-C domains are larger in diameter than the opal-CT fibers, even in those cases in which it is apparent that several fibers overlap one another. The subhedral grain boundaries of the opal-C domains suggest that they grew slower during a later stage of diagenesis. A mottled diffraction contrast associated with moiré fringes characterizes the microstructure of the opal-CT domains.

TEM micrographs revealed that more ordered opal-C domains also occur within opal-CT fibers, as shown in Figure 5G. In this area, several relic opal-CT fibers lie in the image plane. Subhedral nonlamellar domains of opal-C, located within the relic opal-CT fibers, display a strong diffraction contrast. In comparison, diffraction contrast from adjacent regions of the relic fibers is much less intense. The association of newly formed opal-C crystallites of various sizes and the distribution of more ordered cristobalite-type domains within and on existing acicular opal-CT fibers suggest that Ostwald ripening processes promote the formation of more ordered microcrystalline opal in opal-CT porcelanite. As discussed in the next section, tabular crystals of pseudo-orthorhombic low tridymite were identified in another region of one of the opal-CT porcelanite samples.

HRTEM RESULTS

Our HRTEM investigation targeted the characterization of microcrystalline opal species that formed in the matrix of banded opal-CT–quartz chert from the Monterey Formation. Fiber types identified include length-slow opal-C and so-called "lussatite" (length-slow, unidimensionally disordered opal-CT). Opal-CT crystals, characterized by incoherently interstratified lamellar domains, and tabular crystals of pseudo-orthorhombic tridymite were also identified in this study.

Length-slow fibrous opal-C

Two subparallel length-slow opal-C fibers, shown in Figure 6A, were imaged using the low-dose spot-scan protocol. Variation in diffraction contrast in the HRTEM micrograph was produced by overlap of the rastered elec-

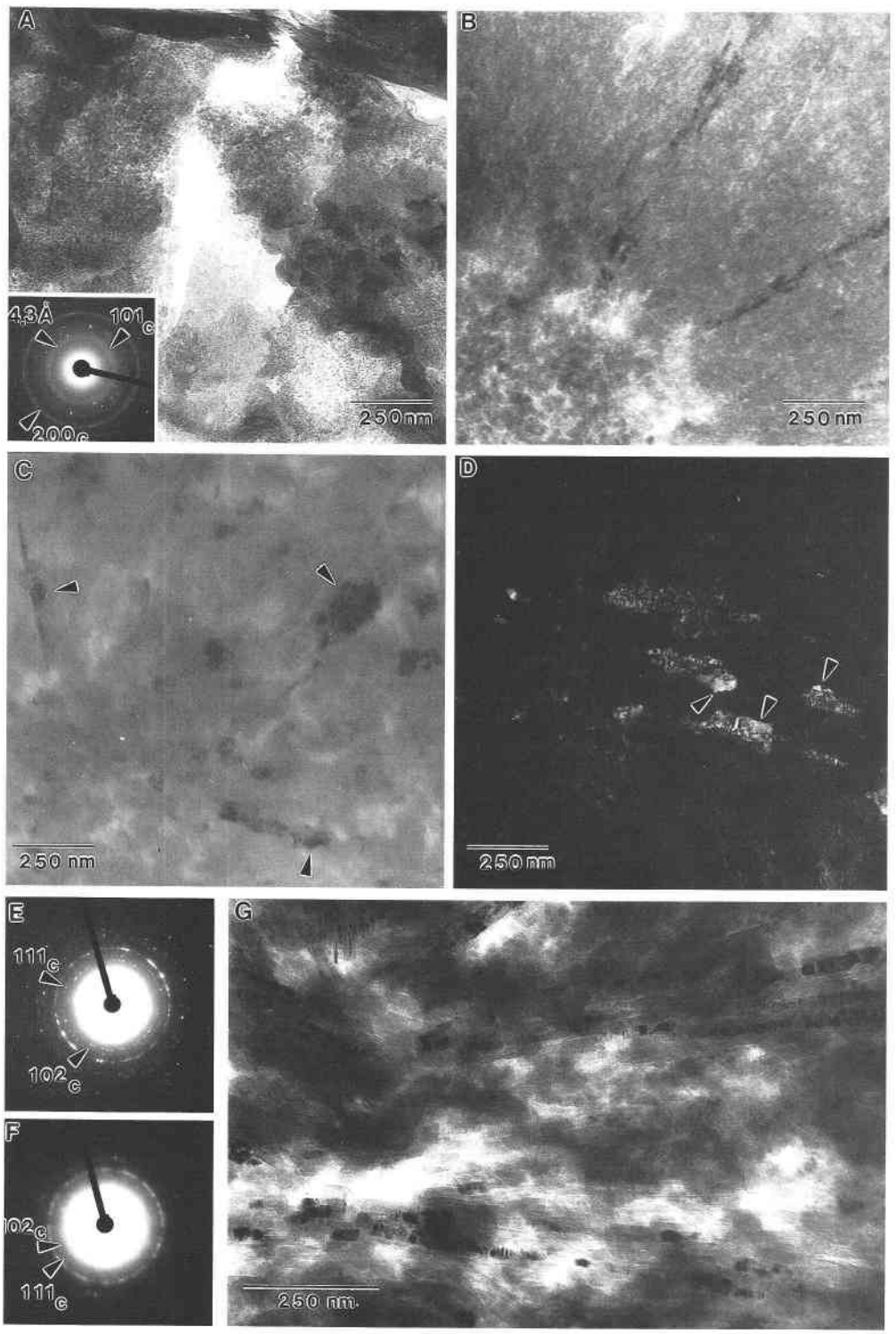

FIGURE 5. Inset in **A** shows SAED pattern of newly formed opal-CT crystallites. Bright-field (BF) TEM micrographs of microcrystalline opal in opal-CT porcelanite show (**A**) dense matrix of opal-CT crystallites, (**B**) opal-CT fibers oriented perpendicular to microfossil cavity infilled with opal-CT crystallites, and (**C**) approximately equidimensional opal-C crystals in area surrounding microfossil cavity and opal-C domains within opal-CT fibers. Dark-field (DF) TEM micrograph shows (**D**) opal-C domains within opal-CT fibers and epitaxial overgrowths of opal-C crystals on opal-CT fibers. (**E** and **F**) SAED patterns corresponding to (**C**) BF TEM micrograph and (**D**) DF TEM micrograph showing additional low cristobalite reflections. (**G**) BF micrograph of opal-C domains within relic opal-CT fibers.

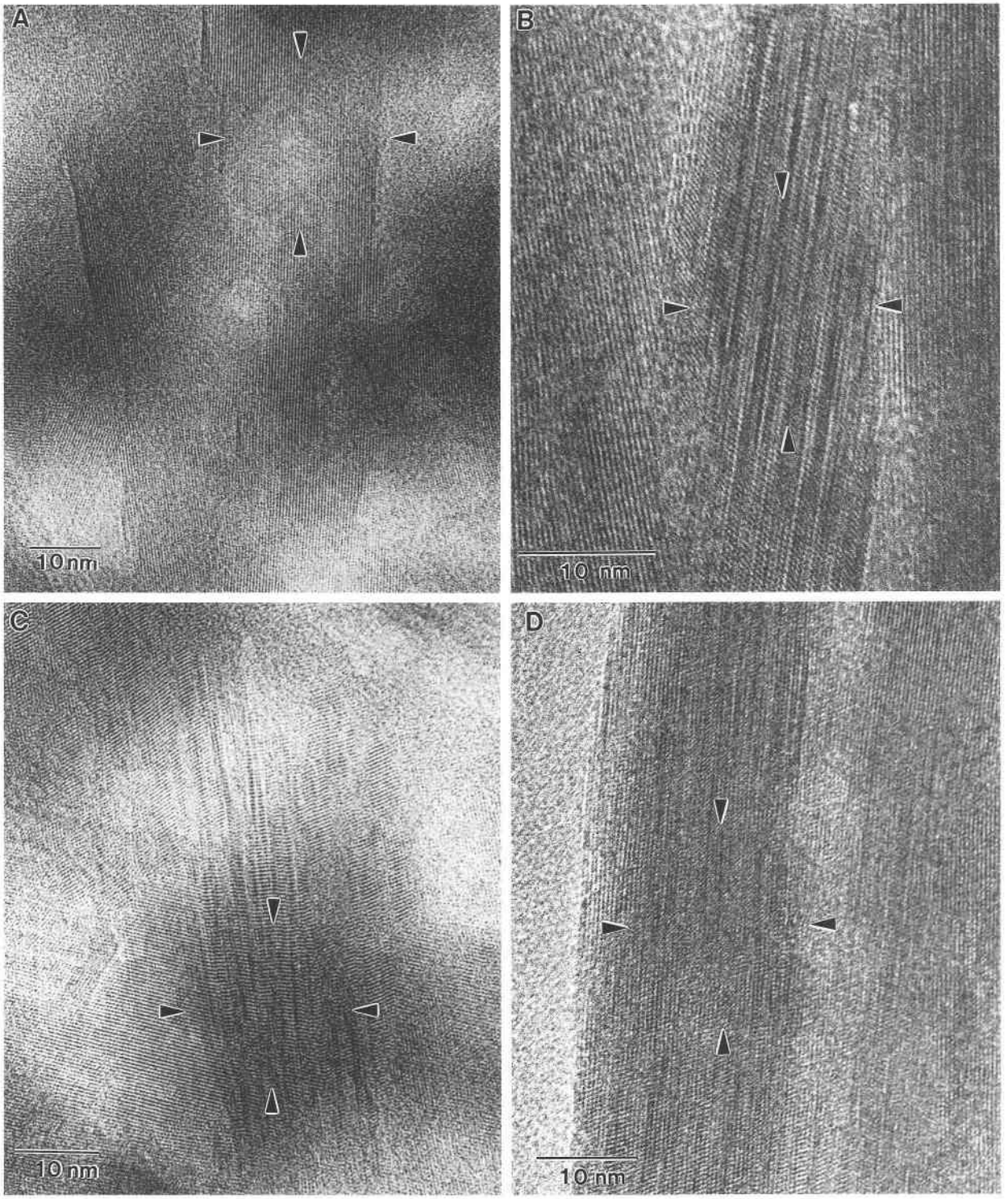

Figure 6. High-resolution TEM micrographs show (**A**) length-slow opal-C fibers, (**B** and **D**) "lussatite" (unidimensionally disordered opal-CT) fibers, and (**C**) incoherently disordered opal-CT crystal. Arrows show area used to produce optical diffractogram (Fig. 7).

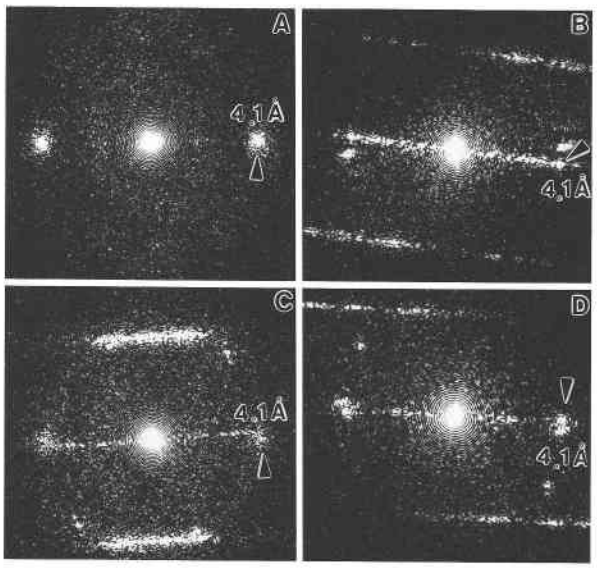

FIGURE 7. Optical diffractograms **A**, **B**, **C**, and **D** correspond to HRTEM micrographs shown in Figures 6A, 6B, 6D, and 6C, respectively.

tron beam. These opal-C fibers are oriented with their fiber axes at a small angle to the HRTEM image plane. The systematic row of reflections in the optical diffractogram (Fig. 7A) of one of the fibers corresponds to a 4.1 Å lattice-fringe spacing. Opal-C fibers that are elongated in a direction perpendicular to the stacking direction of the 4.1 Å lattice planes display length-slow optical character; the fiber axis lies parallel to one of the *a* axes in low cristobalite (e.g., Graetsch et al. 1994). The absence of streaking parallel to the stacking direction in the optical diffractogram indicates that these fibers do not contain a significant number of stacking defects.

Well-ordered crystalline domains located within discrete sections of the opal-C fibers display strong lattice-fringe contrast. These ordered domains are separated by irregularly and elliptically shaped regions that have little, if any, lattice-fringe contrast. Elliptically shaped regions void of diffraction contrast are interpreted to result from radiolytic damage because of their similarity in appearance and character to the black-spot damage that occurs in quartz under irradiation in the transmission electron microscope (e.g., Carter and Kohlstedt 1981). The more irregularly shaped regions, however, appear to be highly strained; lattice fringes, when visible in these regions, are discontinuous or curved. These regions are interpreted to contain a high concentration of defects, the nature of which cannot be determined from an analysis of lattice-fringe HRTEM images. The absence of long-range order along the fiber length is interpreted to contribute to the mottled diffraction contrast observed in many of the fibers of microcrystalline opal shown in the conventional TEM images.

Smaller domains that also display a 4.1 Å lattice-fringe spacing are located in the region where the two fibers diverge from one another. The smaller domains are misoriented with respect to either of the two fiber axes. Misorientation of aggregated crystal nuclei during the early stages of crystal growth is interpreted to cause the subsequent growth of fiber bundles that contain randomly oriented fibers.

Lussatite, length-slow fibrous opal-CT

The microstructure of many opal-CT fibers in banded opal-CT–quartz chert displays a unidimensional stacking disorder oriented perpendicular to the fiber axis, as is characteristic of lussatite (e.g., Flörke et al. 1991; Graetsch et al. 1994). The fiber located in the center of the HRTEM image shown in Figure 6B and the fibers shown in Figure 6D are oriented to display two sets of 4.1 Å lattice fringes. The stacking direction of one set of lattice fringes lies perpendicular to the fiber axis, whereas the stacking direction of another set of lattice fringes is oriented approximately 70° away from the first. This arrangement of lattice fringes would be visible in length-slow low cristobalite fibers if viewed perpendicular to the *a-c* plane (e.g., Graetsch et al. 1994).

In the HRTEM image of the lussatite fiber shown in Figure 6B, it is possible to identify the presence of a significant amount of local disorder at some of the interlamellar boundaries between stacked lamellar domains. Lattice strain at the interlamellar boundaries is evidenced by the presence of curved lattice fringes that lie approximately 70° from the direction of the fiber axis. Some of the lamellar domains, offset by nonintegral multiples of the lattice-fringe spacing (4.1 Å), display an incoherent stacking disorder. The narrow width of the lamellar domains (<15 Å) produces streaking in the optical diffractogram (Fig. 7B). Variation in the lattice-fringe spacing of the lussatite fiber, as evidenced by the diffuse nature of the primary 4.1 Å reflections in the optical diffractogram, indicates the presence of both cristobalite-type and tridymite-type domains. However, the combination of curved lattice fringes at interlamellar boundaries, lattice-fringe offset, and the narrow width of lamellar domains (<20 Å) suggests that cristobalite-type and tridymite-type layers are interstratified within the lamellar domains. An additional set of primary 4.1 Å reflections in the optical diffractogram (Fig. 7B) is produced by an adjacent, subparallel lussatite fiber. The presence of diffuse reflections of ~4 Å and the absence of streaking in the optical diffractogram indicate that stacking disorder in this lussatite fiber occurs with negligible lattice strain.

Longer lussatite fibers shown in Figure 6D also display lamellar diffraction contrast. However, these lussatite fibers contain ordered domains at discrete positions, located along the direction of the fiber axes, that are separated by highly strained regions characterized by a discontinuity in lattice fringes. The highly strained regions are similar to those identified in the opal-C fibers. The aperiodic crystallization of ordered domains that contain variable amounts of lamellar stacking disorder and highly strained regions is interpreted to result from diffusion-

limited transport of pure silica to the growth front. With a decrease in the concentration of silica in the solute, higher concentrations of impurities that have accumulated at the growth front are likely to become incorporated at structural defects located in the highly strained regions or within tridymite-type lamellar domains. Coalescence of closely spaced fibers at a later stage of silicification is evidenced by the presence of discontinuous lattice fringes in the area between adjacent fibers. The optical diffractogram for the region of the lussatite fiber marked in Figure 6D is shown in Figure 7D.

Opal-CT crystals with incoherently interstratified lamellar domains

Opal-CT crystals characterized by incoherently interstratified lamellar domains were identified in both banded opal-CT–quartz chert and opal-CT porcelanite samples. Only a few of these crystals have been identified in the HRTEM images obtained to date. The HRTEM micrograph shown in Figure 6C was produced using the spot-scan, low-dose imaging protocol. In this orientation, it is apparent that the microstructure of these crystals is characterized by lamellar domains stacked in a direction perpendicular to the longest dimension of the crystal. The finite thickness of these lamellar domains produced intense streaking in the optical diffractogram parallel to the direction of stacking disorder (Fig. 7C). Although planar boundaries separate lamellar domains in this variety of opal-CT, neither the domains nor the planar boundaries that separate them continue along the full length of the crystal. The presence of incoherently interstratified lamellar domains caused the crystal to splay and to become wider as it grew. We did not observe crystals with these microstructural characteristics in any other orientation; therefore, it is possible that this crystal type is actually a cross section through a fan of blades or platelets.

Many of the domains in these opal-CT crystals are characterized by a herringbone lattice-fringe pattern produced by the relative difference in orientation of lattice fringes in adjacent domains. The angle between the stacking directions of lattice fringes in adjacent domains varies from 0 to 20°. The stacking direction of one set of lattice fringes lies parallel to the longest dimension of the crystal, whereas the stacking direction of a second set of lattice fringes lies ±20° to the first. Another set of lattice fringes, characterized by a stacking direction that lies perpendicular to the longest dimension of the crystal, can be observed in some of the lamellar domains. In many places, the relative orientation of the two dominant sets of lattice fringes indicates that some of the lamellar domains are twinned, a feature that would produce a herringbone lattice-fringe pattern. The exact nature of these twins was not identified in these opal-CT crystals. Lamellar domains twinned according to the spinel law with a {101} low cristobalite composition plane would produce a similar type of herringbone pattern in HRTEM micrographs, with lattice fringes oriented ±70° to the composition plane. The composition plane of pseudohexagonal twins in pseudo-orthorhombic tridymite also lies parallel to 4.1 Å lattice planes (Ashworth 1989). Because the orientation of the two sets of lattice fringes varies, it is likely that more than one type of twin occurs in these opal-CT crystals.

Tridymite PO-2

Tabular-shaped platelets of pseudo-orthorhombic tridymite were identified in the matrix of one of the opal-CT porcelanite samples. These crystals, less than a few tenths of a micrometer in diameter, are doubly terminated and display a hexagonal morphology (Fig. 8A). Thinner regions of the pseudo-orthorhombic crystals (Fig. 8B) were used to obtain the optical diffractograms shown in Figures 8C and 8D. In this orientation, superstructure reflections resulted from a coherently disordered stacking periodicity along the *c* axis. The spacing of the superstructure reflections (16.4 Å) corresponds to a two-layer polytypic stacking sequence (PO-2). The optical diffractogram also contains hexagonal subcell reflections that are significantly more intense than those produced by the pseudo-orthorhombic superstructure (e.g., Carpenter and Wennemer 1985). It should be noted that powder XRD patterns from this sample do not contain reflections from PO-2 tridymite, suggesting that this silica polymorph may be volumetrically insignificant.

Tridymite crystals interpreted to have precipitated from percolating groundwater during uplift have been identified in cherts from the Onnagawa Formation in Japan (Tada and Iijima 1982). Electron diffraction analysis of siliceous samples from deep-sea cherts by Wilson et al. (1974) revealed that in some crystals the predominant structural component of opal-CT is tridymite rather than cristobalite.

Discussion and conclusions

Our low-dose HRTEM study of lussatite provides direct evidence for the unidimensionally disordered crystallographic model of opal-CT originally proposed by Flörke (1955). HRTEM lattice-fringe images also revealed that in some lussatite fibers, the presence of different types of stacked lamellar domains results in the local distortion of silica tetrahedra at the lamellar boundaries. A significant amount of lattice strain was also identified by HRTEM in several lussatite and opal-C fibers to occur as isolated domains that separate ordered domains located aperiodically along the direction of the fiber axes. We interpret the alternation during growth of ordered domains and highly strained regions as an indication of a transport-limited growth process. The separation or misorientation of ordered domains by highly strained regions results in a mottled diffraction contrast displayed by these fibers when observed using conventional TEM methods. These findings demonstrate how different species of microfibrous opal, characterized by highly strained microstructures and varying amounts and types of stacking disorder, contribute to the end-member structural components noncrystalline opal and tridymite-cristobalite identified by

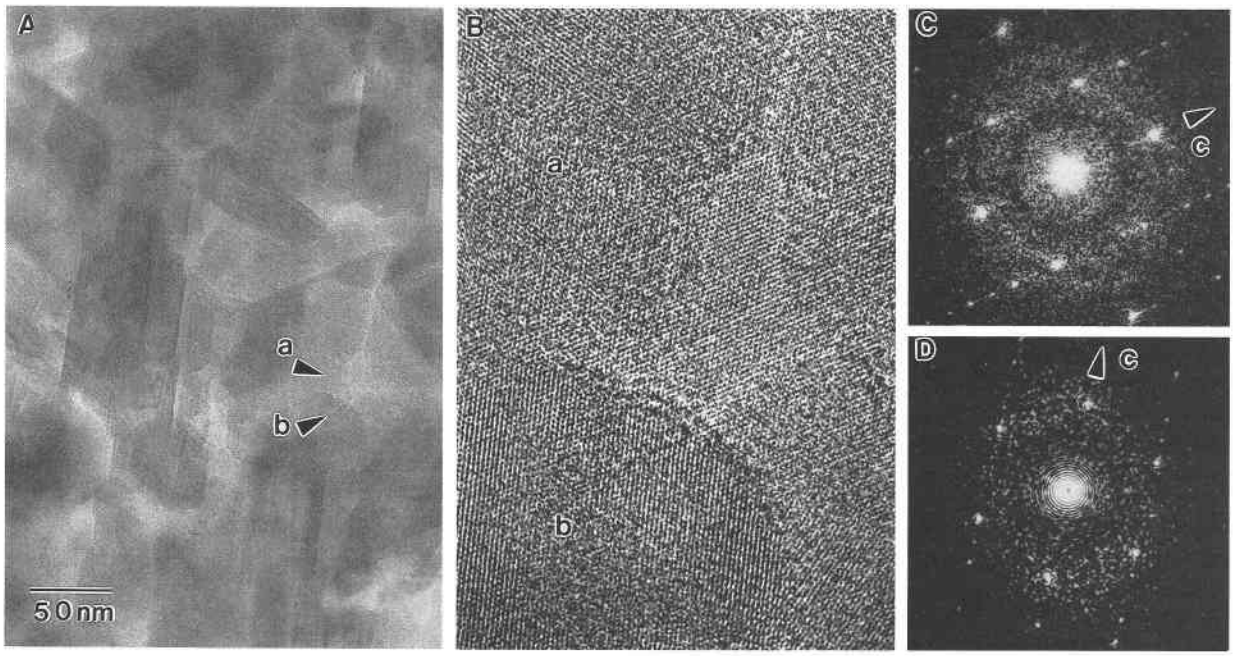

FIGURE 8. (**A**) TEM micrograph of tabular PO-2 tridymite crystals in opal-CT porcelanite. (**B**) High-resolution TEM micrograph of electron-transparent region of TEM foil used to produce **C** and **D** optical diffractograms of PO-2 tridymite crystals showing polytypic stacking periodicity along c^* axis. PO-2 tridymite crystals (labeled a and b) correspond to optical diffractograms **C** and **D**, respectively.

Graetsch et al. (1994) using ^{29}Si MAS NMR and infrared-absorption spectroscopies.

Behl and Garrison (1994) recently showed, on the basis of ^{18}O isotope studies, that opal-CT forms at lower temperatures in opal-CT chert than in opal-CT porcelanite. The authors proposed that the local concentration or addition of silica at sites of enhanced permeability in opal-A diatomite plays a critical role in promoting the early formation of opal-CT. Our TEM investigation of banded opal-CT–quartz chert provides additional evidence that early-formed opal-CT precipitated from concentrated solutions. TEM micrographs revealed that microcrystalline opal occurs as a dense matrix of acicular fibers and various types of fiber-aggregation forms. The precipitation of fiber bundles, rosettes, and embryonic spherulites requires an influx of solution supersaturated with respect to cristobalite but undersaturated with respect to noncrystalline opal to facilitate nucleation and growth of these high-energy crystal forms and the development of fibrous aggregates. Our TEM observations also suggest that many of the so-called "blades" in embryonic opal-CT lepispheres (see Flörke et al. 1975, Fig. 1; Flörke et al. 1976, Figs. 1 and 2) consist of radially arranged fiber bundles. We observed that the growth direction of interpenetrating fibers within embryonic lepispheres may be crystallographically controlled. It is likely that during chertification, the epitaxial precipitation of silica around closely spaced fibers that are arranged in interpenetrating fiber bundles would contribute to the appearance of a bladed morphology in scanning electron micrographs. Our observation that embryonic lepispheres may form from interpenetrating fibrous aggregates also explains the presence of the knobby-shaped protrusions that characterize the outermost edges of blades in many of the opal-CT lepispheres reported in the literature.

On the basis of our TEM observations and microstructural analysis of lattice-fringe images, we propose that many of the fibers in banded opal-CT–quartz chert grew by a transport-limited growth mechanism during early diagenesis. We interpret the limited amount of intracrystalline growth of fibers to be a result of the rapid rate of consumption of pure material from the solution relative to the rate at which impurities near the fibers can be rejected. We believe that the periodic incorporation of adsorbed foreign ions at the growth front, which includes OH and H_2O molecules, also caused the observed separation of crystalline domains by highly strained regions along the fiber-axis direction of many lussatite and opal-C fibers. Our interpretation contrasts with the observations made by Flörke et al. (1990) regarding the growth of hydrothermally synthesized fibrous cristobalite. Flörke et al. (1990) found that synthetic hydrothermal microfibrous opal initially precipitated as octahedral nuclei that developed into fibers as a result of dendritic branching. However, under hydrothermal conditions, high rates of silica transport would be expected to assist in the strong segregation of impurities away from the growth front.

The open-system process of chertification in banded chert (e.g., Behl and Garrison 1994) differs from the in situ diagenetic process that accommodates the formation

of opal-CT in porcelanite (e.g., Isaacs 1982). Our TEM investigation revealed that, in addition to the precipitation of equidimensional opal-CT crystallites, more ordered opal-C crystals precipitate authigenically in opal-CT porcelanite samples that have a relatively high average primary d value (4.11 Å). In opal-CT porcelanite samples that have a smaller average primary d value (4.06 Å), opal-C occurs as epitaxial overgrowths on opal-CT fibers and as euhedral domains within relic fibers of opal-CT.

Our study has also provided new evidence in support of diagenetic solid-state ordering in microcrystalline opal as originally proposed by Murata and Nakata (1974). TEM micrographs revealed that lussatite fibers that occur at the boundaries between microcrystalline opal and microquartz laminae in banded opal-CT–quartz chert are characterized by an increase in the number of ordered lamellar domains. We interpret the presence of an increased number of ordered lamellar domains that are accompanied by an apparent increase in disorder in the interlamellar regions between ordered domains as evidence of solid-state structural reordering. More ordered lamellar domains were also observed to characterize the microstructure of some of the shorter lussatite fibers found in the less pure opal-CT laminae of banded opal-CT–quartz chert. In the short lussatite fibers, however, the lamellar domains continue along the full length of the fibers, which suggests they formed during the initial growth process rather than during a later stage of diagenetic maturation.

Our observation of the heterogeneous nucleation of quartz on microfibrous opal substrates provides insight into the role and relative significance of a solid-state transformation between microfibrous opal and microquartz (e.g., Wenk et al. 1988). Many authors have argued on a theoretical basis that the primary diagenetic silica phase transformations between opal-A, opal-CT, and quartz occur exclusively by a series of dissolution-reprecipitation reactions (e.g., Williams et al. 1985). Although ^{18}O isotope studies have indicated that the primary diagenetic silica phase transformations occur as a result of dissolution and reprecipitation processes (Murata et al. 1977), our TEM investigation revealed that the earliest formed quartz crystals in banded opal-CT–quartz chert precipitate as epitaxial overgrowths on microfibrous opal. The epitaxial growth of quartz on microfibrous opal would be favored when the concentration of silica in the interstitial pore fluid lies between the solubility of cristobalite and quartz. Our TEM and HRTEM study suggests that during the period of diagenesis in which opal-CT becomes more ordered, prior to quartz formation, opal-C may precipitate homogeneously from solution and heterogeneously on microcrystalline opal substrates. Also, opal-CT may structurally reorder, and the earliest formed quartz crystals may precipitate as epitaxial overgrowths on microfibrous opal substrates. Once the concentration of silica in the interstitial pore fluid reaches the solubility of quartz, we believe that the role of epitaxy and the subsequent topotaxial conversion of opal-CT to quartz diminish, and that the reaction then proceeds predominantly by a dissolution-reprecipitation transformation mechanism.

Acknowledgments

This article is based on doctoral research by S.L.C. conducted at the Geology and Geophysics Department of the University of California, Berkeley, under the guidance of H.-R.W. The Donors of The Petroleum Research Fund, administered by the American Chemical Society, are acknowledged for the support of this research (grant PRF24344-AC2 to H.-R.W.). Additional support was generously provided to S.L.C. by an Achievement Rewards for College Scientists Scholarship. The authors are grateful to G.D. Guthrie Jr., P.J. Heaney, C.M. Isaacs, and an anonymous reviewer for their constructive comments. The research relied on access to facilities at the Geology and Geophysics Department of the University of California, Berkeley (NSF grant EAR-9104605 to H.-R.W.), and at Lawrence Berkeley National Laboratory, at both the Life Sciences Division and the National Center for Electron Microscopy (U.S. Department of Energy contract DE-AC-03-76SF00098). Samples were kindly provided by C.M. Isaacs, R.W. Murray, and K.A. Pisciotto.

References cited

Ashworth, J.R. (1989) Transmission electron microscopy of coexisting low-tridymite polymorphs. Mineralogical Magazine, 53, 89–97.

Baronnet, A. (1982) Ostwald ripening in solution: The case of calcite and mica. Estudios Geologicos, 38, 185–198.

Baur, W.H. (1977) Silicon-oxygen bond lengths, bridging angles Si-O-Si and synthetic low tridymite. Acta Crystallographica, B33, 2615–2619.

Behl, R.J., and Garrison, R.E. (1994) The origin of chert in the Monterey Formation of California (USA). In A. Iijima, A. Abed, and R. Garrison, Eds., Siliceous, phosphatic and glauconitic sediments of the Tertiary and Mesozoic: Proceedings of the 29th International Geological Congress, Part C, p. 101–132. VSP, Ultrecht.

Bramlette, M.N. (1946) The Monterey Formation of California and the origin of its siliceous rocks. U.S. Geologic Survey Professional Paper 212, 57 p.

Buseck, P., Cowley, J., and Eyring, L. (1988) High-resolution transmission electron microscope and associated techniques, 645 p. Oxford University Press, New York.

Cady, S.L., Wenk, H.-R., Kilaas, R., and Barber, D.J. (1993) Enantiomorphism and planar defects in length-fast chalcedony. In J.N. Boland and J.D. Fitz Gerald, Eds., Defects and processes in the solid state: Geoscience applications, developments in petrology 14, p. 383–400. Elsevier, Amsterdam.

Carpenter, M.A., and Wennemer, M. (1985) Characterization of synthetic tridymites by transmission electron microscopy. American Mineralogist, 70, 517–528.

Carter, C.B., and Kohlstedt, D.L. (1981) Electron irradiation damage in natural quartz grains. Physics and Chemistry of Minerals, 7, 110–116.

Das, G., and Mitchell, T.E. (1974) Electron irradiation damage in quartz. Radiation Effects, 23, 49–52.

Dollase, W.A. (1965) Reinvestigation of the structure of low cristobalite. Zeitschrift für Kristallographie, 121, 369–377.

Dollase, W.A., and Baur, W.H. (1976) The superstructure of meteoritic low tridymite solved by computer simulation. American Mineralogist, 61, 971–978.

Downing, K.H. (1991) Spot-scan imaging in transmission electron microscopy. Science, 251, 53–59.

Downing, K.H., Koster, A.J., and Typke, D. (1992) Overview of computer-aided electron microscopy. Ultramicroscopy, 46, 189–197.

Dunham, J.B., and Blake, G.H. (1987) Guide to coastal outcrops of the Monterey Formation of Western Santa Barbara County, California. Pacific Section Society of Economic Paleontologists and Mineralogists, 53, 36 p.

Flörke, O.W. (1955) Die Modifikationen von SiO_2. Fortschritte der Mineralogie, 44, 181–230 (in German).

———(1967) The structure of $AlPO_4$ and SiO_2. In G.H. Stewart, Ed., Science of ceramics: Proceedings of the 3rd Conference of the British

Ceramic Society and the Nederlandse Keramische Vereniging, University of Bristol, July 5–8, 1965, p. 13–27. Academic Press, London, U.K.

Flörke, O.W., Jones, J.B., and Segnit, E.R. (1975) Opal-CT crystals. Neues Jahrbuch für Mineralogie Monatshefte, 8, 369–377.

Flörke, O.W., Hollmann, R., Rad, U.v., and Rösch, R. (1976) Intergrowth and twinning in opal-CT lepispheres. Contributions to Mineralogy and Petrology, 58, 235–242.

Flörke, O.W., Graetsch, H., and Jones, J.B. (1990) Hydrothermal deposition of cristobalite. Neues Jahrbuch für Mineralogie Monatshefte, 2, 81–95.

Flörke, O.W., Graetsch, H., Martin, B., Röller, K., and Wirth, R. (1991) Nomenclature of micro- and non-crystalline silica minerals, based on structure and microstructure. Neues Jahrbuch für Mineralogie Abhandlungen, 163-1, 19–42.

Garrison, R.E., Douglas, R.G., Pisciotto, K.A., Isaacs, C.M., and Ingle, J.C., Eds. (1981) The Monterey Formation and related siliceous rocks of California. Pacific Section Society for Economic Paleontologists and Mineralogists Special Publication 15, 327 p.

Garrison, R.E., and Ingle, J.C. (1985) Sedimentology, depositional environments, and biostratigraphic studies. In The geochemical and paleoenvironmental history of the Monterey Formation; Sediments and hydrocarbons. Data Volume, 2, p. 21–98. Global Geochemistry Corporation, Canoga Park, California.

Graetsch, H., Flörke, O.W., and Miehe, G. (1985) The nature of water in chalcedony and opal-C from Brazilian agate geodes. Physics and Chemistry of Minerals, 12, 300–306.

———(1987) Structural defects in microcrystalline silica. Physics and Chemistry of Minerals, 14, 249–257.

Graetsch, H., and Flörke, O.W. (1991) X-ray powder diffraction patterns and phase relationship of tridymite modifications. Zeitschrift für Kristallographie, 195, 31–48.

Graetsch, H., Gies, H., and Topalovic, I. (1994) NMR, XRD and IR study on microcrystalline opals. Physics and Chemistry of Minerals, 21, 166–175.

Guthrie, G.D., Jr., Bish, D.L. and Reynolds, R.C., Jr. (1995) Modeling the X-ray diffraction pattern of opal-CT. American Mineralogist, 80, 869–872.

Heaney, P.J. (1994) Structure and chemistry of the low-pressure silica polymorphs. In Mineralogical Society of America Reviews in Mineralogy, 29, 1–40.

Hein, J.R., Scholl, D.W., Barron, J.A., Jones, M.G., and Miller, J. (1978) Diagenesis of Late Cenozoic diatomaceous deposits and formation of the bottom simulating reflector in the southern Bering Sea. Sedimentology, 25, 155–181.

Hein, J.R., Vallier, T.L., and Allan, M.A. (1981) Chert petrology and geochemistry, mid-Pacific mountains and Hess Rise, Leg 62. In Initial Reports of the Deep Sea Drilling Project, 62, 711–748. U.S. Government Printing Office, Washington, DC.

Hesse, R. (1988) Origin of chert: Diagenesis of biogenic siliceous sediments. Geoscience Canada, 15, 171–192.

Hinman, N.W. (1990) Chemical factors influencing the rates and sequences of silica phase transitions: Effects of organic constituents. Geochimica et Cosmochimica Acta, 54, 1563–1574.

Hobbs, L.W. (1979) Radiation damage in electron microscopy of inorganic solids. Ultramicroscopy, 3, 381–386.

———(1985) Radiation effects in the electron microscope. EMSA Bulletin, 15-1, 51–63.

Isaacs, C.M. (1981a) Outline of diagenesis in the Monterey Formation examined laterally along the Santa Barbara Coast, California. In C.M. Isaacs, Ed., Guide to the Monterey Formation in the California coastal area, Ventura to San Luis Obispo, p. 25–38. Pacific Section American Association of Petroleum Geologists Special Publication 52.

———(1981b) Field characterization of rocks in the Monterey Formation along the coast near Santa Barbara, California. In C.M. Isaacs, Ed., Guide to the Monterey Formation in the California coastal area, Ventura to San Luis Obispo, p. 39–53. Pacific Section American Association of Petroleum Geologists 52.

———(1981c) Porosity reduction during diagenesis of the Monterey Formation, Santa Barbara coastal area, California. In R.E. Garrison, R.G. Douglas, K.E. Pisciotto, C.M. Isaacs, and J.C. Ingle Jr., Eds., The Monterey Formation and related siliceous rocks of California, p. 257–272. Pacific Section Society of Economic Paleontologists and Mineralogists Special Publication 15.

———(1982) Influence of rock composition on kinetics of silica phase changes in the Monterey Formation, Santa Barbara area, California. Geology, 10, 304–308.

Isaacs, C.M., and Garrison, R.E., Eds. (1983) Petroleum generation and occurrence in the Miocene Monterey Formation, California. Pacific Section Society of Economic Paleontologists and Mineralogists 33, 228 p.

Isaacs, C.M., Pisciotto, K.A., and Garrison, R.E. (1983) Facies and diagenesis of the Miocene Monterey Formation, California: A summary. In Siliceous Deposits in the Pacific Region, Developments in Sedimentology, 36, 247–282.

Jagodzinski, H. (1949a) Eindimensionale Fehlordnung in Kristallen und ihr Einfluss auf die Röntgeninterferenzen: I. Berechnung des Fehlordnungsgrades aus den Röntgenintensitäten. Acta Crystallographica, 2, 201–207 (in German).

———(1949b) Eindimensionale Fehlordnung in Kristallen und ihr Einfluss auf die Röntgeninterferenzen: II. Berechnung des fehlgeordneten dichtesten Kugelpackungen mit Wechselwirkungen der Reichweite 3*. Acta Crystallographica, 2, 208–214 (in German).

———(1949c) Eindimensionale Fehlordnung in Kristallen und ihr Einfluss auf die Röntgeninterferenzen: III. Vergleich der Berechnungen mit experimentellen Ergebnissen. Acta Crystallographica, 2, 298–304 (in German).

Jagodzinski, H., and Laves, F. (1948) Eindimensional fehlgeordnete Kristallgitter. Schweizerische Mineralogische und Petrographische Mitteilungen, 28, 456–467 (in German).

Jones, J.B., and Segnit, E.R. (1971) The nature of opal: I. Nomenclature and constituent phases. Journal of the Geological Society of Australia, 18-1, 57–68.

Kastner, M., Keene, J.B., and Gieskes, J.M. (1977) Diagenesis of siliceous oozes: I. Chemical controls on the rate of opal-A to opal-CT transformation: An experimental study. Geochimica et Cosmochimica Acta, 41, 1041–1059.

Kastner, M., and Gieskes, J.M. (1983) Opal-A to opal-CT transformation: A kinetic study. In A. Iijima, J.R. Hein, and R. Siever, Eds., Siliceous deposits in the Pacific Region, developments in sedimentology 36, p. 211–227. Elsevier, Amsterdam.

Kato, K., and Nukui, A. (1976) The structure of monoclinic low-tridymite. Acta Crystallographica, B32, 2486–2491 (in German).

Keene, J.B. (1975) Cherts and porcelanites from the North Pacific, DSDP, Leg 32. In Initial Reports of the Deep Sea Drilling Project, 32, 425–507. U.S. Government Printing Office, Washington, DC.

Keller, M.A., and Isaacs, C.M. (1985) An evaluation of temperature scales for silica diagenesis in diatomaceous sequences including a new approach based on the Miocene Monterey Formation, California. Geo-Marine Letters, 5, 31–35.

Keller, M.A., and McGowen, M.K. (1990) Miocene and Oligocene petroleum reservoirs of the Santa Maria and Santa Barbara–Ventura Basins, California, 400 p. Society of Economic Paleontologists and Mineralogists Core Workshop 14.

Konnert, J.H., and Appleman, D.E. (1978) The crystal structure of low tridymite. Acta Crystallographica, B34, 391–403.

Langer, K., and Flörke, O.W. (1974) Near infrared absorption spectra (4,000–9,000 cm^{-1}) of opals and the role of "water" in the $SiO_2 \cdot nH_2O$ minerals. Fortschritte der Mineralogie, 52, 17–51.

Löns, J., and Hoffman, W. (1987) Zur Kristallstruktur der inkommensurablen Raumtemperaturphase des Tridymits (abs.). Zeitschrift für Kristallographie, 178, 141–143 (in German).

Mizutani, S. (1966) Transformation of silica under hydrothermal conditions. Journal of Earth Sciences, Nagoya University, 14, 56–88.

———(1977) Progressive ordering of cristobalitic silica in the early stage of diagenesis. Contributions to Mineralogy and Petrology, 61, 129–140.

Morse, J.W., and Casey, W.H. (1988) Ostwald processes and mineral paragenesis in sediments. American Journal of Science, 288, 537–560.

Murata, K.J., and Nakata, J.K. (1974) Cristobalitic stage in the diagenesis of diatomaceous shale. Science, 184, 567–568.

Murata, K.J., and Larson, R.R. (1975) Diagenesis of Miocene siliceous

shales, Temblor Range, California. Journal of Research of the U.S. Geological Survey, 3, 553–566.

Murata, K.J., and Randall, R.G. (1975) Silica mineralogy and structure of the Monterey Shale, Temblor Range, California. Journal of Research of the U.S. Geological Survey, 3, 567–572.

Murata, K.J., Friedman, I., and Gleason, J.D. (1977) Oxygen isotope relations between diagenetic silica minerals in Monterey Shale, Temblor Range, California. American Journal of Science, 277, 259–272.

Nukui, A., and Nakazawa, H. (1980) Polytypism in tridymite. Journal of Mineral Society of Japan, 14, Special Volume 2, 14, 364–386 (in Japanese).

Nukui, A., and Flörke, O.W. (1987) Three tridymite structural modifications and cristobalite intergrown in one crystal. American Mineralogist, 72, 167–169.

Oehler, J.H. (1975) Origin and distribution of silica lepispheres in porcelanite from the Monterey Formation of California. Journal of Sedimentary Petrology, 45-1, 252–257.

Pascucci, M.R., Hutchison, J.L., and Hobbs, L.W. (1983) The metamict transformation in alpha-quartz. Radiation Effects, 74, 219–226.

Peacor, D.R. (1973) High-temperature single-crystal study of the cristobalite inversion. Zeitschrift für Kristallographie, 138, 274–298.

Pisciotto, K.A. (1981) Diagenetic trends in the siliceous facies of the Monterey Shale in the Santa Maria region, California. Sedimentology, 28, 547–571.

Pisciotto, K.A., and Garrison, R.E. (1981) Lithofacies and depositional environments of the Monterey Formation, California. In R.E. Garrison, R.G. Douglas, K.E. Pisciotto, C.M. Isaacs, and J.C. Ingle Jr., Eds., The Monterey Formation and related siliceous rocks of California, p. 97–122. Pacific Section Society of Economic Paleontologists and Mineralogists Special Publication 15.

Rad, U.v., and Rösch, H. (1972) Mineralogy and origin of clay minerals, silica and authigenic silicates in Leg 14 sediments. In Initial Reports of the Deep Sea Drilling Project, 14, 725–751. U.S. Government Printing Office, Washington, DC.

Schneider, H., and Flörke, O.W. (1986) High-temperature transformation of tridymite single crystals to cristobalite. Zeitschrift für Kristallographie, 175, 165–176.

Schwalbach, J.R., and Bohacs, K.M. (1993) Sequence stratigraphy in fine-grained rocks: Examples from the Monterey Formation. Pacific Section Society for Sedimentary Petrologists and Mineralogists 70, 7–19.

Steefel, C.I., and Van Cappellen, P. (1990) A new kinetic approach to modeling water-rock interaction: The role of nucleation, precursors, and Ostwald ripening. Geochimica et Cosmochimica Acta, 54, 2657–2677.

Tada, R., and Iijima, A. (1982) Identification of mixtures of opaline silica phases and its implication for silica diagenesis. In A. Iijima, J.R. Hein, and R.Siever, Eds., Siliceous deposits in the Pacific Region, developments in sedimentology 36, p. 229–245. Elsevier, Amsterdam.

Weaver, F.M., and Wise, S.W., Jr. (1972) Ultramorphology of deep sea cristobalitic chert. Nature, 237, 56–57.

Wenk, H.-R., Shaffer, S.J., and Van Tendeloo, G. (1988) Planar defects in low temperature quartz. Physica Status Solidi, A-107, 799–805.

Wennemer, M., and Thompson, A.B. (1984) Tridymite polymorphs and polytypes. Schweizerische Mineralogische und Petrographische Mitteilungen, 64, 335–354.

Williams, L.A., and Crerar, D.A. (1985) Silica diagenesis: II. General mechanisms. Journal of Sedimentary Petrology, 55-3, 312–321.

Williams, L.A., Parks, G.A., and Crerar, D.A. (1985) Silica diagenesis: I. Solubility controls. Journal of Sedimentary Petrology, 55-3, 301–311.

Williams, R., and Fisher, H. (1970) Electron microscopy of tobacco mosaic virus under conditions of minimal beam exposure. Journal of Molecular Biology, 52, 121–123.

Wilson, J.J., Russell, J.D., and Tait, J.M. (1974) A new interpretation of the structure of disordered alpha-cristobalite. Contributions to Mineralogy and Petrology, 47, 1–6.

Wise, S.W., Jr., Buie, B.F., and Weaver, F.M. (1972) Chemically precipitated cristobalite and the origin of chert. Eclogae Geologicae Helvetiae, 65, 157–163.

Manuscript received June 1, 1995
Manuscript accepted July 15, 1996